Chapter 7

Greenish-yellow emission from rare-earth free Li^+ doped zinc vanadate phosphor

In this chapter, we present synthesis and spectral study of $Zn_{(3-x)}Li_x(VO_4)_2$ (x=0, 0.01, 0.02, 0.03) samples. The crystallinity of $Zn_3(VO_4)_2$ is improved by doping Li^+ ions and is supported by the augmentation in crystallite size. The XPS analysis ascertains the V^{+5} oxidation state of vanadium thereby confirming the single-phase of the phosphors. The Li^+ ion doping enhances the broadband excitation in the near UV region and emission band of $Zn_3(VO_4)_2$ in the visible region with stokes shift of 9517.3 cm^{-1}. The thermal stability of the emission spectra is also discussed in the chapter. Thus, with the broadband near-UV excitation and greenish-yellow emission, the Li^+ doped zinc vanadate phosphor can be utilized with near-UV LED chips for the realization of white light.

7.1 Introduction

In chapter 6, we studied zinc vanadate phosphors as a rare-earth-free host material for White light-emitting diodes (wLEDs) application and luminescence enhancement by Bi^{3+} doping. However, in the previous chapter, we were unable to synthesize the pure orthorhombic phase of the $Zn_3(VO_4)_2$ phosphors. In this chapter, we discuss the synthesis and luminescence properties for Li^+ doped $Zn_3(VO_4)_2$ phosphors for wLED application. The wLEDs have received a lot of attention recently in the field of solid-state lighting industry because of their significant advantages such as high luminous efficacy, eco-friendliness, enhanced optical power, longer operational lifetime, and energy efficacy [217]. The commercial wLEDs are fabricated by coating Ce^{3+}:YAG yellow phosphor over the blue chips [53,91]. However, such white light lacks sufficient distribution of power in the red region of visible spectrum which results in high correlated color temperature (CCT > 4,500 K) and poor color rendering index (CRI<75) [58]. To address this issue, researchers have proposed several rare-earth-doped single host materials for wLED application [112,218–220]. But the approaches for high-cost refining, separation, and purification of all the rare-earth materials make them expensive [221]. Therefore, there is a need to develop rare-earth-free self-luminescent phosphors for lighting and other optoelectronic applications. In this regard, materials such as vanadate and tungstate have been studied for their use in solid-state lighting.

Vanadate compounds are potential materials for application in the fields of electrochemistry, solid-state lighting devices, catalysis, and optical lasers [140,222–226]. The findings of yttrium vanadate prompted the synthesis and study of many vanadate phosphors for their self-luminescence property [227]. The self-luminescence property of vanadate compounds has made them advantageous over commercial rare-earth-activated phosphors.

The emission spectra of many vanadate compounds cover the full visible range and also have near Ultraviolet (UV) excitation [30–32]. The near UV absorption of vanadate phosphors overlaps the emission spectrum of the commercially available near UV LED chips used in wLED fabrication and therefore vanadate phosphors can be is used with near UV chips for the realization of white light [33,34]. The luminescence of vanadate compounds is owed to their VO_4 tetrahedral with T_d symmetry [30]. In VO_4 tetrahedral, the charge transfer from 2p orbitals of O^{2-} to 3d orbitals of V^{5+} takes place, thereby yielding a broadband emission spectrum that covers the whole visible range [35]. Thus, this self-luminescence property along with a low-cost synthesis process and energy efficiency adds to the advantage of vanadate phosphors over conventional phosphors [30–32].

Among different vanadate phosphors, zinc vanadate ($Zn_3(VO_4)_2$) phosphor has been explored as an effective solar energy transfer material, photo-catalyst, and white light-emitting phosphor [10-12]. Nakajima et al. have widely investigated the $M_3V_2O_8$ (M= Zn, Ba, Sr, and Ca) material system and the correlation between the structural properties and Quantum efficiency (QE) of $M_3V_2O_8$ vanadates with isolated VO_4 tetrahedra [25–27]. They concluded that the weak interaction between V^{5+} and M^{2+} ions and the strong interaction between the V ions in the $M_3V_2O_8$ crystal system strongly influence the QE of these phosphors. Their findings reveal that the $Zn_3(VO_4)_2$ phosphor has the highest emission and QE compared to other $M_3V_2O_8$ (M= Sr, Ba, and Ca) phosphors. Moreover, the QE of $Zn_3(VO_4)_2$ is also more than many reported garnet vanadate phosphors [28]. Thus, the choice of $Zn_3(VO_4)_2$ over other $M_3V_2O_8$ (M= Sr, Ba, and Ca) phosphors is clear.

There are few reports on the single-phase $Zn_3(VO_4)_2$ phosphor. This is because vanadium has multiple oxidation states and $Zn_3(VO_4)_2$ is sensitive to the synthesis process and annealing temperature. Previous reports on $Zn_3(VO_4)_2$ phosphor conclude that an additional

monoclinic phase ($Zn_2V_2O_7$) is formed along with the primary orthorhombic phase [199,203,222,228,229]. Nakajima et al. have published a synthesis of $Zn_3(VO_4)_2$ by the high-temperature solid-state method [25,26]. Shibing et al. have reported the synthesis of $Zn_3(VO_4)_2$ microparticles, which require 10 h annealing in the N_2 atmosphere [230]. Therefore, there is a need to synthesize single-phase $Zn_3(VO_4)_2$ phosphor by the energy-efficient method. In this chapter, we discuss a facile citrate sol-gel method for the synthesis of single-phase $Zn_{(3-x)}Li_x(VO_4)_2$ (x=0, 0.01, 0.02, 0.03) phosphors, where the dried gel was annealed at 700^0C for 4 h. With low annealing temperature and less annealing time, our synthesis technique is energy efficient as compared to earlier reported techniques. Moreover, in the sol-gel method, the reagents are mixed homogenously in an aqueous solution. The single phase of prepared phosphors is validated by the Rietveld refinement of the x-ray diffraction (XRD) data and is supported by Fourier transform infrared (FTIR) spectroscopy analysis. Moreover, the V^{5+} oxidation state of the vanadium is validated by X-ray photoelectron spectroscopy (XPS).

The influence of Li^+ ion on the luminescence properties of various host materials and rare-earth elements has been explored widely [104,209,231,232]. The smaller ionic size of the Li^+ ion allows it to occupy substitutional as well as interstitial sites, thereby tailoring the local crystal field and thus increasing the emission intensity of the material. Many reports propose that the incorporation of Li^+ ion results in a significant alteration in the crystallinity of the host phosphor [209,231]. These reports encourage the use of Li^+ ions for improving luminescence properties. The effect of Li^+ on the luminescence and structural property of the zinc vanadate is not investigated to date and is thus explored by us.

7.2 Material and methods

7.2.1 Phosphor synthesis

The precursors for the phosphor synthesis were $Zn(NO_3)_2.6H_2O$ (99%, SRL chemicals), NH_4VO_3 (Sigma-Aldrich, 99%), and $LiNO_3$ (Sigma-Aldrich, 99.99%). The phosphors were synthesized by the sol-gel method using citric acid (Sigma-Aldrich, 99.5%). The $Zn_{(3-x)}Li_x(VO_4)_2$ (x=0, 0.01, 0.02, 0.03) samples are assigned with code names L0, L1, L2, and L3, respectively. The synthesis process is discussed in chapter 2 and presented schematically in Fig. 7.1.

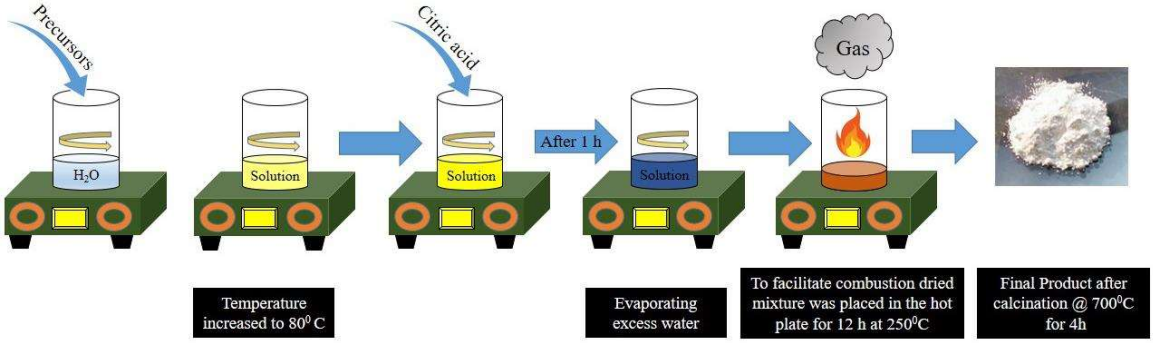

Fig. 7.1 Schematic of the synthesis process.

7.2.2 Characterisation

The XRD data of the phosphors were obtained using Rigaku-MiniFlex 600 desktop x-ray diffraction system having with Cu K_α radiation source (λ=1.54Å). The phase purity and crystal structure was validated by the use of FULLPROF software [119]. The vibrational modes of the phosphors were determined from FTIR scans, obtained using a JASCO FT/IR 4600 spectrometer coupled with the Attenuated total reflection (ATR) setup, which includes a diamond disc as an internal reflection component. Prior to each sample examination, the spectrum of air was employed as a backdrop. Field emission scanning electron microscopy is utilized to inspect the morphology of the produced samples analysis, which is performed using Nova Nano SEM 450, USA. The average particle was calculated

using ImageJ computer software. The UV-Vis absorption spectroscopy of the prepared powder samples was performed with the integrating sphere setup attached to the JASCO V770 spectrophotometer. The UV-Vis absorption spectra were recorded in absorbance mode after baseline correction using barium sulphate. The Photoluminescence emission (PL), photoluminescence excitation (PLE), and Temperature-dependent PL (TDPL) spectra were fetched using the Horiba Fluorolog-3 spectrophotometer. The PL and PLE spectrum of all the prepared phosphors were recorded for the slit width fixed at 1 nm. The PL lifetime measurement was done using the FLS920 spectrometer (Edinburgh Instruments) equipped with a 60W xenon flash lamp. The absolute PL quantum yield measurement was done with the help of Horiba PTI QuantaMaster-400 fluorescence spectrometer equipped with an integrating sphere. Thermo Fischer Scientific ESCALAB Xi X-ray photoelectron spectrometer was used for XPS measurements.

7.3 Results and discussion

7.3.1 Structural analysis

7.3.1.1 XRD study

The formation of solid solution and crystalline phase of the samples are authenticated by the XRD data analysis. The XRD study confirms the orthorhombic phase (JCPDS card no. 34-0378) of the prepared phosphors with symmetry described by the space-group of Cmca. The Rietveld refined XRD patterns of all produced phosphors are shown in Fig. 7.2 (a). Some of the prominent peaks for L0 are indexed in Fig. 7.2 (a). It is observed that the most intense peak for the host sample (L0) is located at 34.92^0 which is indexed as (221). Further, by increasing the Li^+ doping, the intensity of peaks at 15.4^0 and 31.04^0 indexed as (020) and (040), respectively, is increased compared to the (221) peak. The height of the diffraction peak is influenced by the preferential crystal orientation and therefore the

increased height of the (020) and (040) plane compared to the (221) plane indicates that the particles become more oriented towards (020) and (040) plane with increasing Li^+ concentration. Moreover, no extra impurity peak corresponding to Li^+ is observed. The crystal structure obtained after refinement and modeled using VESTA software is depicted in Fig. 7.2 (b). The Zn^{2+} ions are present in the two octahedral sites, while V^{5+} ions occupy tetrahedral sites. The Zn^{2+} ions with 2/*m* symmetry have two different bond lengths, while Zn ions with *m* symmetry have three different bond lengths with oxygen [35]. Table 7.1 summarises the atomic coordinates of the component atoms, lattice parameters, unit cell volume, and bond lengths derived following Rietveld refinement. Fig. 7.2(c) presents the variation in the full-width half maximum (FWHM) for the (020) peak of all the phosphors. It is observed that the FWHM of the peak is decreased with Li^+ doping which indicates increased crystallinity of the phosphors [231].

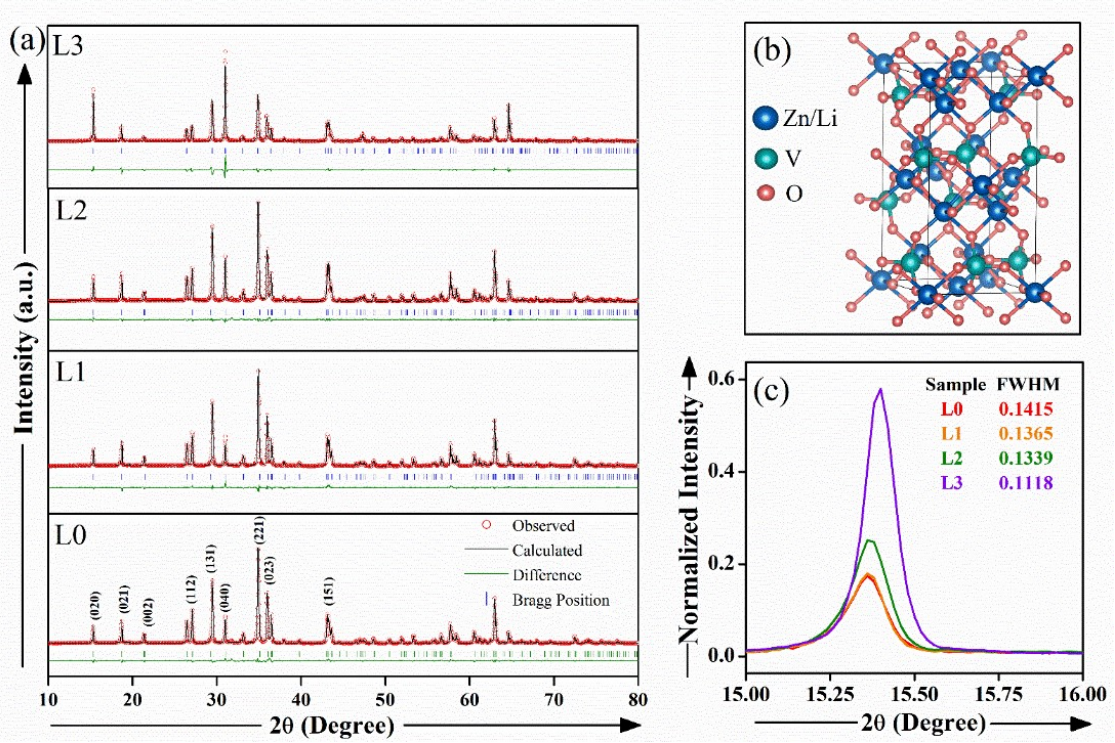

Fig. 7.2 (a) Rietveld refined XRD patterns of samples. **(b)** Crystal structure of the samples based on refinement data. **(c)** The alteration in the peak intensity and FWHM of (020) peak in 2**θ** for all prepared samples.

The Williamson-Hall (W-H) equation is utilized for approximating the average crystallite size (D) and lattice strain (ϵ) of the phosphors. The Williamson-Hall equation is given by the equation 7.1 [35],

$$\beta_{hkl}cos\theta = 4\epsilon sin\theta + \frac{K\lambda}{D}, \tag{7.1}$$

Where the sum of microstrain broadening and crystallite size broadening is given by the resultant peak broadening (β_{hkl}), K resembles the crystallite shape factor, λ is the wavelength of the radiation, and θ denotes the Bragg angle. Fig. 7.3 presents the W-H plot for all the phosphors. The crystallite size (D) obtained from the slope of the linearly fitted line for L0, L1, L2, and L3 is 58 nm, 60 nm, 64 nm, and 69 nm, respectively. An augmentation in crystallite size value suggests that Li^+ ions favor the growth of crystallites and increase crystallinity [209,231,232]. The improvement in the crystallinity help in enhancing the emission intensity. The lattice strain is obtained from the intercept of the fitted straight line. The obtained value of lattice strain for L0, L1, L2, and L3 is 3.84×10^{-4}, 3.60×10^{-4}, 6.34×10^{-4}, and 9.86×10^{-4}, respectively.

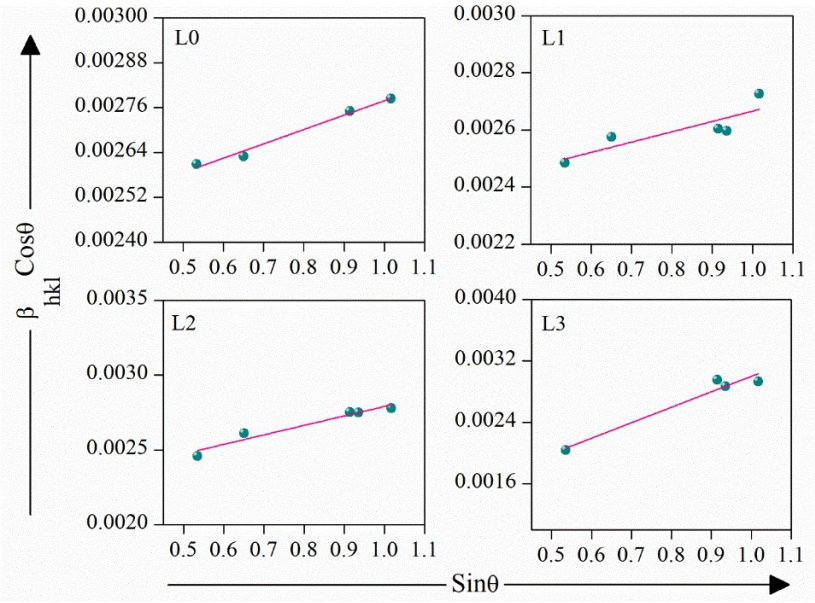

Fig. 7.3 Williamson-Hall plot for all the prepared phosphors.

Table 7.1 Structural parameters for all the phosphors derived after Rietveld refinement of their individual XRD patterns.

Parameters	L0	L1	L2	L3
Atomic positions (x,y,z):				
Zn1/Li1	(0, 0, 0)	(0, 0, 0)	(0, 0, 0)	(0, 0, 0)
Zn2/Li2	(0.25, 0.136, 0.25)	(0.25, 0.136, 0.25)	(0.25, 0.134, 0.25)	(0.25, 0.127, 0.25)
V	(0, 0.377, 0.122)	(0, 0.377, 0.121)	(0, 0.377, 0.120)	(0, 0.382, 0.119)
O1	(0, 0.250, 0.230)	(0, 0.251, 0.228)	(0, 0.244, 0.235)	(0, 0.238, 0.238)
O2	(0, 1.000, 0.246)	(0, 0.996, 0.239)	(0, 0.999, 0.240)	(0, 0.991, 0.233)
O3	(0.222, 0.379, 0.006)	(0.216, 0.379, 0.007)	(0.215, 0.381, 0.003)	(0.215, 0.388, 0.005)
Angles (α, β, γ) in degree	(90, 90, 90)	(90, 90, 90)	(90, 90, 90)	(90, 90, 90)
Lattice parameters (Å)				
a	6.114	6.112	6.114	6.116
b	11.530	11.527	11.527	11.522
c	8.301	8.300	8.303	8.305
Unit cell volume ($Å^3$)	585.26	584.86	585.24	585.30
Bond lengths (Å)				
(Zn1-O2)	2.050(5)	1.992(0)	1.999(3)	1.942(0)
(Zn1-O3)	2.196(3)	2.222(0)	2.214(0)	2.163(0)
(Zn2-O2)	2.190(3)	2.221(0)	2.187(0)	2.194(0)
(Zn2-O1)	2.025(3)	2.031(0)	1.986(0)	1.992(0)
(Zn2-O3)	2.144(3)	2.157(0)	2.123(3)	2.137(0)
(V-O1)	1.714(4)	1.699(0)	1.809(0)	1.929(0)
(V-O2)	1.787(4)	1.789(0)	1.809(0)	1.753(0)
(V-O3)	1.663(3)	1.627(0)	1.636(0)	1.626(0)
$R_{Factors}$				
R_p	8.32	8.95	6.92	10.6
R_{wp}	9.81	9.76	9.31	13.0
χ^2	3.13	3.05	5.14	12.3

7.3.1.2 FTIR spectroscopy analysis

The vibrational bands of phosphors are detected and analysed using FTIR spectrum. The FTIR spectra of un-doped and Li^+ doped $Zn_3(VO_4)_2$ in the wavenumber range of 360 cm^{-1} to 3000 cm^{-1} are depicted in Fig. 7.4 and the band assignment for the respective wavenumber range is arranged in Table 7.2. The band in the region 410-426 cm^{-1} for L0 is ascribed to Zn-O stretching vibrations from ZnO_6 octahedra [230,233]. It is observed that there is a shift in Zn-O stretching vibrations towards the higher wavenumber side for doped samples, which is attributed to Li^+ doping in the host. The intense broadband around 516-724 cm^{-1} is ascribed to VO_4 tetrahedral vibrational modes [230]. The band observed at 782 cm^{-1} corresponds to Zn-O-V and V-O-V asymmetric vibrations [224,233]. The vibrational band around 808-852 cm^{-1} is accredited to V-O stretching vibration [211]. The vibrational bands attributed to VO_4 groups remain unaltered with Li^+ doping. The observed vibrational bands support the formation of the orthorhombic crystal structure of $Zn_3(VO_4)_2$ and are in accordance with previously stated values [35,233]. The band at 2363 cm^{-1} corresponds to CO asymmetric stretching vibration [35].

Table 7.2 Vibrational modes assigned to different wavenumber bands observed in FTIR spectrum of samples.

Vibrational bands present in the phosphors (cm^{-1})				**Vibrational mode assignments**
L0	**L1**	**L2**	**L3**	
411-425	411-425	418-429	421-431	Zn-O stretching
516-724	516-724	516-724	516-724	VO_4 vibrational modes
782	782	782	782	Zn-O-V asymmetric and V-O-V vibrations
808-850	808-850	808-850	808-850	V-O stretching vibration
2364	2364	2364	2364	CO asymmetric stretching

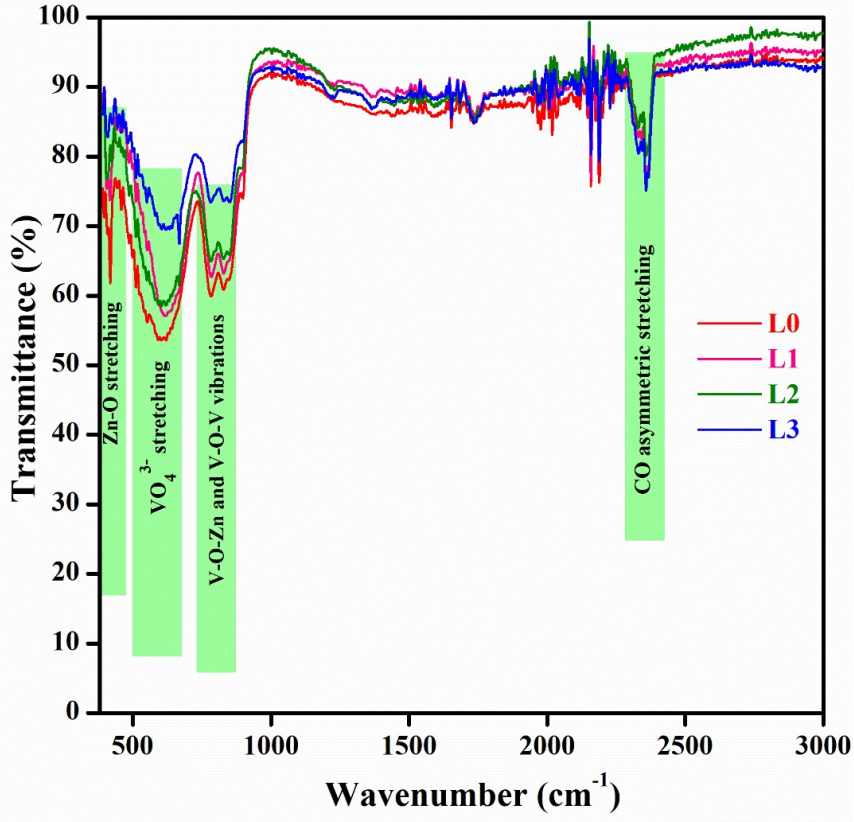

Fig. 7.4 FTIR spectra of all prepared phosphors.

7.3.1.3 FE-SEM analysis

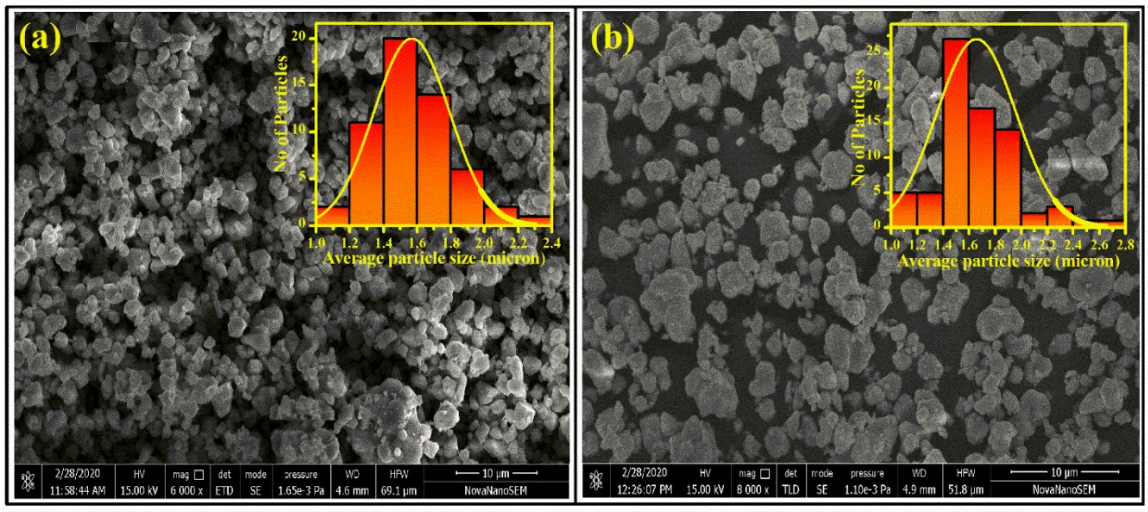

Fig. 7.5 FE-SEM micrographs of **(a)** L0 and **(b)** L2

The influence of Li^+ doping on the morphology of the zinc vanadate is investigated by FE-SEM study. The FE-SEM images of L0 and L2 samples are depicted in Fig. 7.5 (a) and (b), respectively. The particles in both samples are well distributed and exhibit little

aggregation. The average particle size of L0 and L2 is 1.56 μm and 1.65 μm, respectively. Morphological analysis demonstrates that the average particle size is increased by Li^+ doping.

7.3.1.4 XPS analysis

XPS spectra is utilized to analyse the chemical composition and validation of oxidation states of the elements present on the surface of the sample. All XPS data from all elements were charge adjusted for C1s. (~284.6 eV). The survey scan depicted the Fig. 7.6 (a) for the L2 sample confirms the presence of all prominent peaks corresponding to Zn, V, and O. All peaks in the survey scan are assigned per the national institute of standard technology (NIST) database. The survey scan also validates that there is no additional contaminant in the sample other than carbon. The carbon peak is present because of its absorption on the surface of the sample during air exposure. Fig. 7.6 (b), (c), (d), and (e) depicts the XPS spectra of V (2p), Li (1s), Zn (2p), and O (1s) for L2 sample. The high-resolution core-level spectrum in Fig. 7.6 (b), shows peaks corresponding to V (2p) having BE of ~516.97 eV ($2p_{3/2}$) and ~524.47 eV ($2p_{1/2}$) with doublet separation (Δ) of about ~7.4 eV. This confirms that the vanadium present in the sample is in the V^{5+} oxidation state [224,230,233,234]. The XPS spectrum of Li (1s) confirms the presence of Li 1s peak at 54.37 eV [148,235]. The symmetric peak corresponding to Zn (2p) has a core BE of ~1021.37 eV ($2p_{3/2}$) and ~1044.47 eV ($2p_{1/2}$), corroborating that Zn is in Zn^{2+} oxidation state [7,224,230]. The peak at ~529.97 eV corresponds to O (1s) [7,234]. The O1s peak is de-convoluted into two peaks at ~529.95 eV and 531.46 eV, which is accredited to lattice oxygen and surface adsorbed oxygen (i.e. O^-, O_2^-, O_2^{2-}), respectively [234]. The details of XPS spectra confirm that the pure phase of $Zn_3(VO_4)_2$ is formed.

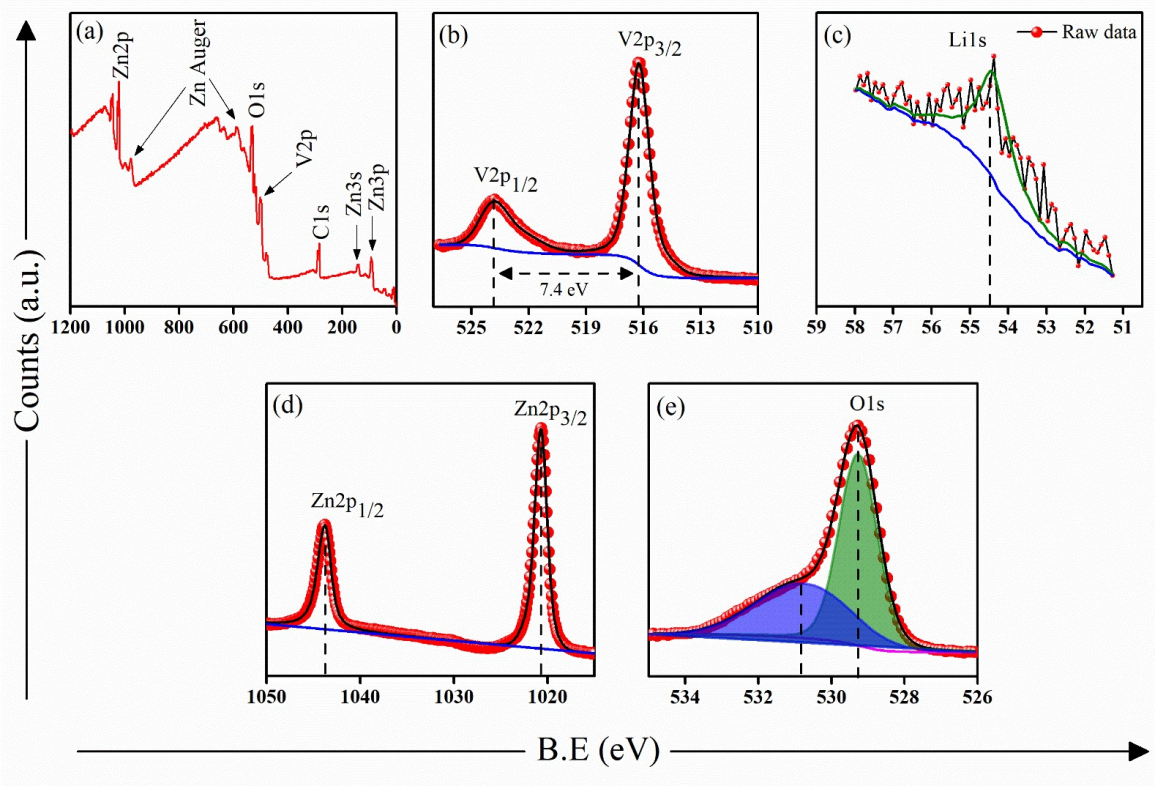

Fig. 7.6 (a) XPS survey scan for L2. XPS spectra of **(b)** V 2p, **(c)** Li 1s, **(d)** Zn 2p, **(e)** O 1s for L2.

7.3.2 Optical study

7.3.2.1 UV-Vis absorption analysis

Fig. 7.7 presents the absorption spectrum of the samples. The absorption band of the prepared phosphors occurs in the near UV region from 300 nm to 450 nm and is centered at 375 nm. The strong absorption in the near UV region ascertains that the prepared phosphors have a strong affinity to absorb near UV photons. The doping of Li^+ has not shifted the peak position of the absorption band. The broad absorption peak is attributed to the ligand to the metal charge transfer band (CTB). The CTB is formed as a result of the charge transfer from O^{2-} to V^{5+} in $[VO_4]$ tetrahedral. The absorption CTB is broadened after Li^+ doping.

The bandgap energy (E_g) for all the phosphors can be evaluated using the following Tauc relation [130]:

$$\alpha h\vartheta = A(h\vartheta - E_g)^n, \tag{7.2}$$

Where α denotes the absorption coefficient and $h\vartheta$ is the photon energy. The $Zn_3(VO_4)_2$ phosphor has a direct allowed electronic transition and therefore n is taken to be ½ [130]. The bandgap of all the phosphors is determined by the x-intercept of the extrapolated linear part of $(\alpha h\vartheta)^2$ versus $(h\vartheta)$ plot and is presented in the inset of Fig. 7.7. The bandgap energy of L0 is estimated to be 2.96 eV and a slight increment in bandgap is observed with Li^+ doping in the host lattice.

The doping-induced disorder in the $Zn_3(VO_4)_2$ can be validated by examining the variation in Urbach energy (E_u). The E_u is evaluated by the following equation 7.3 [23],

$$\alpha = \alpha_0 e^{\left(\frac{h\vartheta}{E_u}\right)} \tag{7.3}$$

Where α_0 is a constant. The E_u is evaluated from the reciprocal of the slope of the linear part of $\ln(\alpha)$ vs $h\vartheta$ plot. The $\ln(\alpha)$ vs. $h\vartheta$ plot for L0 is depicted in Fig. 7.7 (b) and the inset shows the variation in Urbach energy. The E_u for L0 is 0.42 eV and decreases with Li^+ doping. The decrease in E_u with Li^+ doping is a good indication of the increased crystallinity of the samples [35,213].

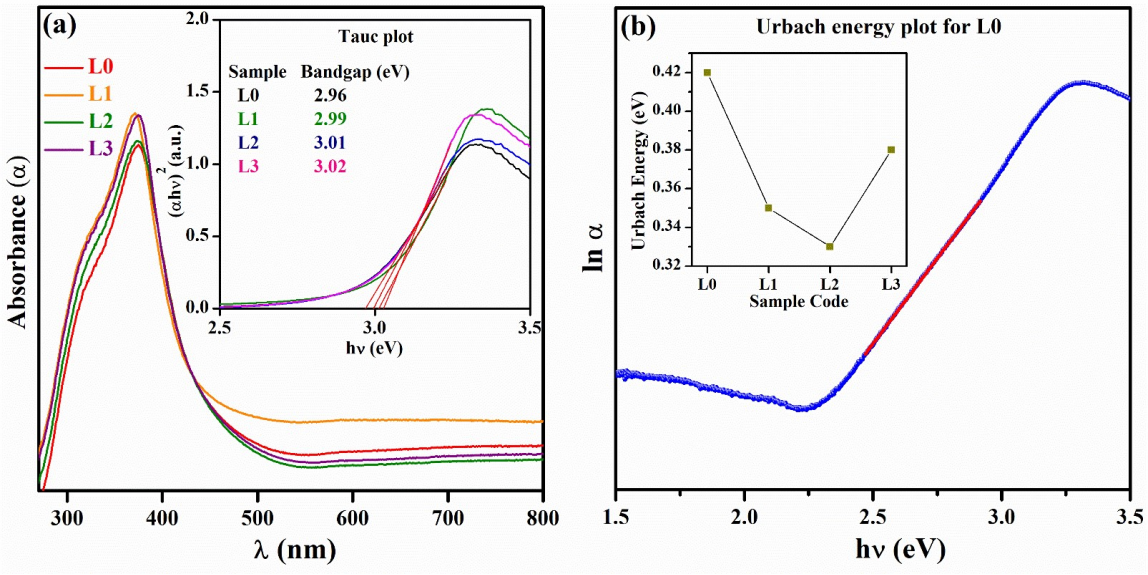

Fig. 7.7 (a) Absorbance spectrum of the samples. Inset shows Tauc plot and bandgap of all the phosphors. **(b)** Urbach energy plot for L0. The fluctuation of Urbach energy with Li^+ doped phosphors is depicted in the inset of **(b)**.

7.3.2.2 Photoluminescence analysis

The PLE spectrum for $Zn_3(VO_4)_2$ and Li^+ doped $Zn_3(VO_4)_2$ samples, examined at 542 nm emission wavelength is presented in Fig. 7.8 (a). The PLE spectrum for all the phosphors exhibits similar absorption broadband ranging from 280 nm to 400 nm. The absorption band in vanadate compounds is attributed to $(VO_4)^{3-}$ groups [30,236]. The molecular orbitals of a V^{5+} ion with T_d symmetry comprise a ground state $^1A_1$, and four excited states, whose energies lie in the order of $^1T_2 > {}^1T_1 > {}^3T_2 \sim {}^3T_1$, as depicted in Fig. 7.9 (e) [31,236]. The Deconvoluted Gaussian fitting of the PLE spectrum for L0 and L2 are shown in Fig. 7.9 (a) and (c), respectively. The Deconvoluted PLE spectrum for L0 exhibit three absorption bands centered at 3.32 eV (Ex1), 3.55 eV (Ex2), and 4.02 eV (Ex3). Not much variation in the peak position of Ex1, Ex2, and Ex3 peaks for L2 is observed but they have slightly increased FWHM as compared to L0 peaks. The Ex3 band is ascribed to $^1A_1 \rightarrow {}^1T_2$ electronic transition and the Ex2 band along with the shoulder Ex1 band corresponds to $^1A_1 \rightarrow {}^1T_1$ electronic transition [30,31,236,237]. It is observed that there is a rise in the PLE

spectrum of Li^+ doped $Zn_3(VO_4)_2$ as compared to undoped $Zn_3(VO_4)_2$. The inset in Fig. 7.8 (a) depicts the variation of PLE spectrum intensity. The near UV excitation is essential for white light LED device application as it overlaps with the emission band of commercial near UV LED chips. Thus, together with near UV LED chips, the Li^+ doped $Zn_3(VO_4)_2$ phosphors can be utilized in wLED applications.

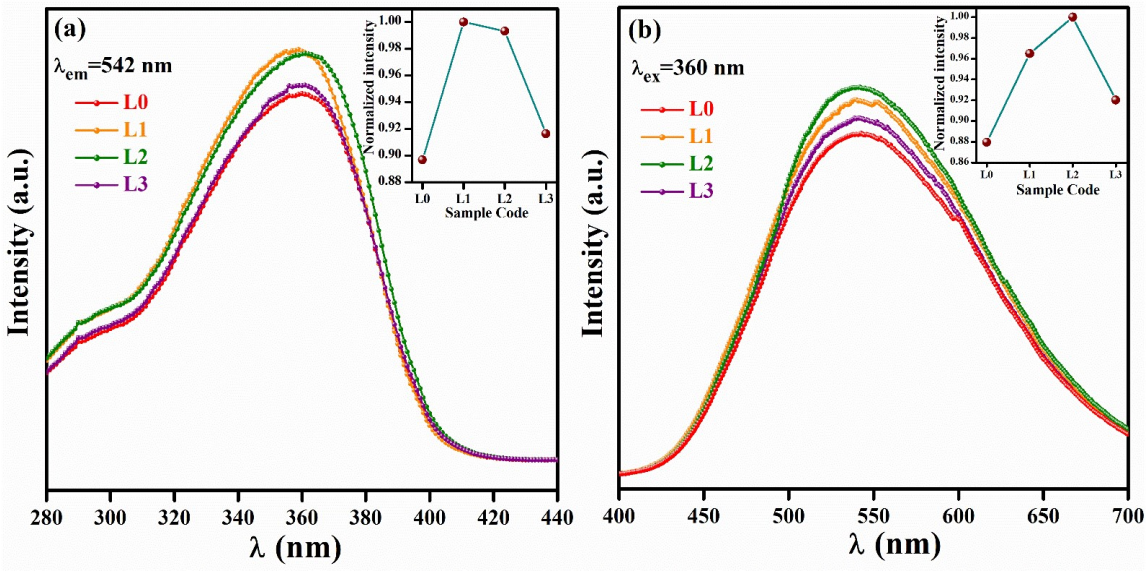

Fig. 7.8 (a) PLE spectra of the phosphors examined at 542 nm emission wavelength. Inset shows the variation of PLE spectrum intensity. **(b)** PL spectra of the prepared phosphors monitored at 360 nm excitation wavelength. Inset shows the variation of PLE spectrum intensity.

Fig. 7.8 (b) depicts the PL spectrum for $Zn_3(VO_4)_2$ and Li^+ doped $Zn_3(VO_4)_2$ samples examined at 360 nm emission wavelength. The PL spectrum for all the phosphors exhibits similar absorption broadband ranging from 400 nm to 700 nm and centered at 542 nm, which is attributed to the charge transfer from the O 2p orbital to the vacant 3d orbital of V^{5+} ion. The emission broadband is attributed to electronic transitions of $(VO_4)^{3-}$ groups, depicted in Fig. 7.9 (e). The deconvoluted Gaussian fitting of the PL spectrum for L0 and L2 are depicted in Fig. 7.9 (b) and (d), respectively. The deconvoluted PL spectrum for L0 exhibits two emission bands centered at 2.09 eV (Em1) and 2.37 eV (Em2), which corresponds to $^3T_1 \rightarrow {}^1A_1$ and $^3T_2 \rightarrow {}^1A_1$ electronic transitions, respectively [238]. In

comparison to L0, the peak position of Em1 and Em2 bands for L2 are red-shifted with the Em1 band overlapping with the Em2 band. The Stokes shift, ΔS, is the energy gap between the excitation edge and the emission band edge. The evaluated ΔS for L0 is 9436.68 cm^{-1} and for L2 it is 9517.33 cm^{-1}. The value of ΔS for L0 and L2 is greater than the commercial phosphors and other reported vanadate phosphors [237,239]. The phosphors with large ΔS values provide white-light emission with uniform hue, high CRI and it reduces self-quenching that results from self-absorption in phosphors [237]. Thus, L0 and L2 phosphors have large ΔS values, which is beneficial for white-light indoor illumination.

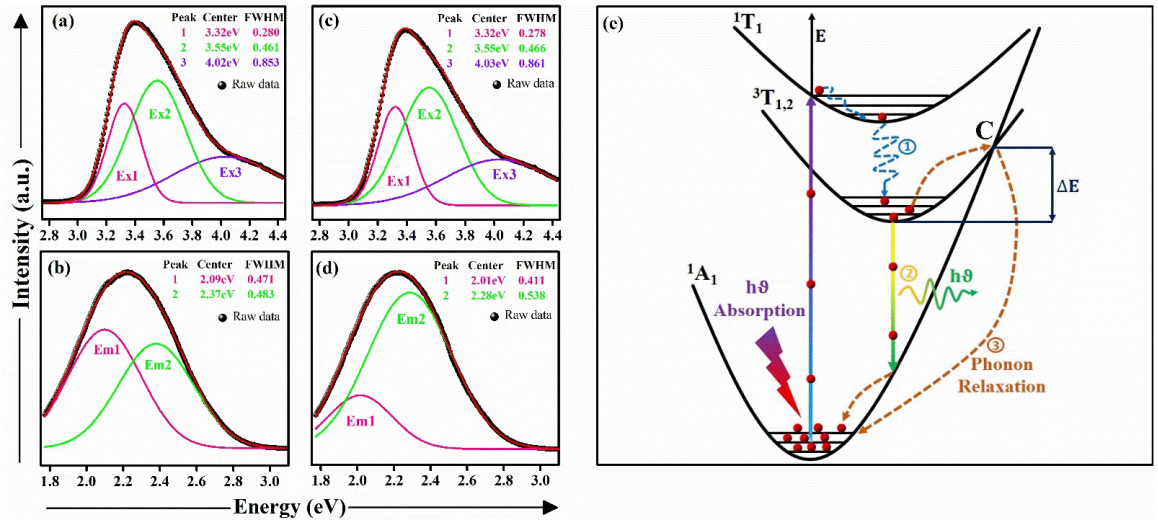

Fig. 7.9 Deconvoluted excitation peak **(a)** and emission peak **(b)** for L0. Deconvoluted excitation peak **(c)** and emission peak **(d)** for L2. **(e)** Configurational coordinate diagram for understanding absorption, florescence, and thermal quenching phenomenon.

7.3.2.3 Role of Li^+ in enhancing the PL intensity

As shown in Fig. 7.8 (b), the PL emission of Li^+ doped $Zn_3(VO_4)_2$ is enhanced as compared to undoped $Zn_3(VO_4)_2$. In perfect VO_4 tetrahedral T_d symmetry, the luminescence process ($^3T_1$,$^3T_2$→$^1A_1$) is forbidden by the spin selection rule. However, in crystal lattices such as $Zn_3(VO_4)_2$, the T_d symmetry is distorted and $^3T_1$→$^1A_1$ and $^3T_2$→$^1A_1$ electronic transitions become partially allowed [199]. The doping of Li^+ ions in $Zn_3(VO_4)_2$ lattice creates variation in the crystal lattice field surrounding the $(VO_4)^{3-}$ groups owing to the difference in ionic

radius of Zn^{2+} and Li^+ ions. This may consequently influence the spin-orbit coupling and distort VO_4 tetrahedron even more from the ideal thereby increasing the luminescence in Li^+ doped $Zn_3(VO_4)_2$ [199]. The increase in emission intensity of L2 compared to L0 is also attributed to the increase in crystallinity, improved crystallite size, and increase in particle size after Li^+ doping. The XRD study reveals that the crystallinity of the host sample is improved with Li^+ doping. The improved crystallinity contributes toward the PL enhancement. The defect centers present on the surface of the particles act as quenching centers for the excited ions, as these defects absorb some of the energy and then prompt ions to relax non-radiatively to their ground state. Thus, with the increase in defect centers, the non-radiative relaxation of ions also increases. It is observed that the increased crystallinity helps in increasing the particle size of the phosphors and therefore decreases the surface-to-volume ratio [23]. As more defect centers are present on the surface of the particles, the decrease in the total surface area of the particle decreases the interaction between the defect centers and the ions. Therefore, the overall number of radiative ions in the crystallites increases thereby increasing the emission intensity [23,121,209,231]. The increase in PLE intensity also contributes to the increase in PL intensity after Li^+ doping. The emission intensity decreases for the L3 sample as a further increase in Li^+ content prompts Li^+ ions to occupy interstitial sites, which creates defects in the crystal and therefore leads to luminescence quenching.

7.3.2.4 Decay curve analysis

The PL decay curves of L0 and L2 phosphors recorded upon 360 nm excitation and 542 nm emission are depicted in Fig. 7.10 (a) and (b), respectively.

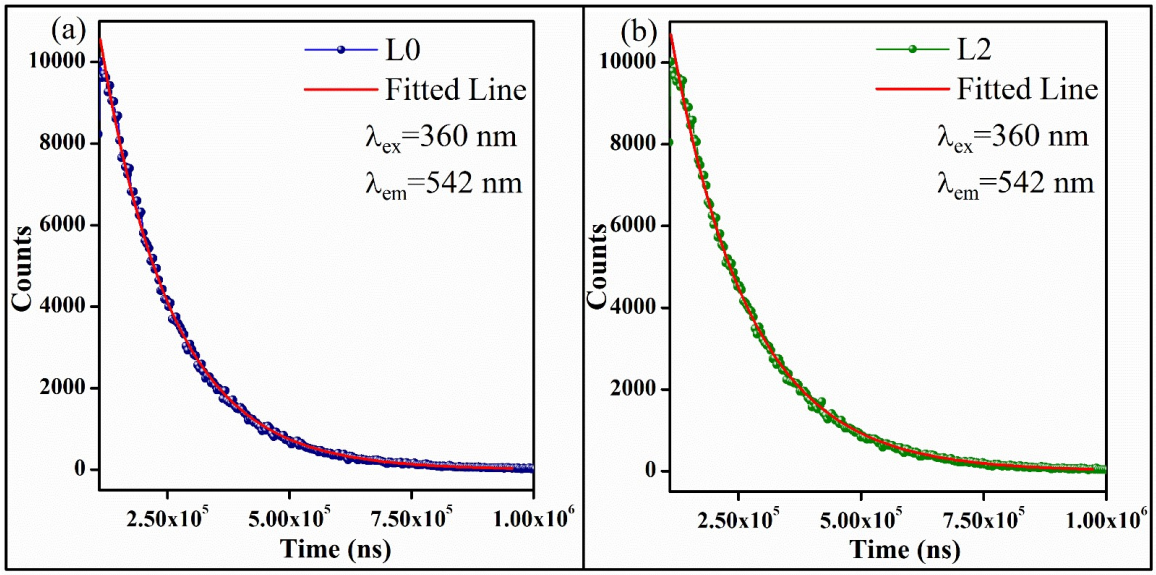

Fig. 7.10 PL decay curves of **(a)** L0 and **(b)** L2 samples, recorded upon 360 nm excitation and 542 nm emission.

The decay curves were examined by fitting them with the single exponential function as determined by the following equation 7.4 [150],

$$I(t) = I_0 exp\left(-\frac{t}{\tau}\right) \tag{7.4}$$

Where, τ is the lifetime of Em1 and Em2 emission bands accredited to the electronic transitions of the $[VO_4]^{3-}$ group. The value of τ for L0 and L2 phosphors is 146 µs and 158 µs, respectively. Thus, it is observed that the lifetime is increased after Li^+ doping. The increased lifetime is attributed to the improved crystallinity in the L2 phosphor. The defect centers operate as luminescence quenchers because the emitting ions lose part of their energy to these defect centers and revert non-radiatively to the ground state. The improvement in crystallinity in the L2 phosphor is an indication of the reduction of defect centers. Thus, by improvement in crystallinity, the probability of non-radiative relaxation of the emitting ions is reduced and the average lifetime of emitting ions is increased. [139,140,142,150,209]. It has also been discovered that the average particle size has grown after 2% Li^+ co-doping. The increase in particle size reduces the surface-to-volume ratio and the

overall grain boundaries. As the defect centers are comparatively more on the surface, therefore with the decrease in surface area and the overall grain boundaries, the number of emitting ions interacting with them also decreases, and the average lifetime of emitting ions increases [139,150]. The analysis of decay curves validates improvement in crystallinity which consecutively supports the increase in the emission intensity of $Zn_3(VO_4)_2$ phosphor in the presence of Li^+ ions.

7.3.2.5 CIE and CCT analysis

The Commission Intentional de I'eclairage (CIE) chromaticity coordinates for L0 and L2 are plotted in the CIE diagram depicted in Fig. 7.11.

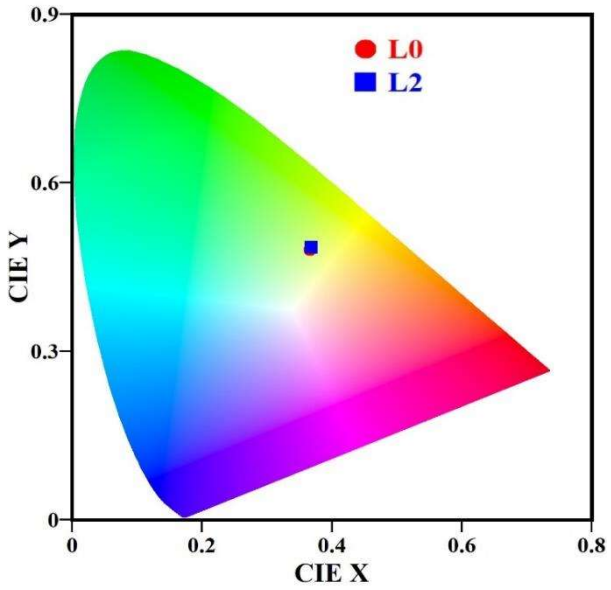

Fig. 7.11 Chromaticity diagram depicting CIE coordinates of L0 and L2 phosphors.

The evaluated CIE coordinates (x, y) for L0 and L2 are (0.366, 0.481) and (0.368, 0.485), respectively. As presented in the CIE diagram, the overall emission of the prepared phosphors is greenish-yellow. The value of color correlated temperature (CCT) has been estimated using the following McCAMY's expression [200,231],

$$CCT = 5520.33 - 6823n + 3525n^2 - 449n^3 \quad (7.5)$$

Where $n = \frac{(x-x_e)}{(y-y_e)}$ is the inverse slope line, (x, y) is the CIE coordinates, and (x_e, y_e) are the chromaticity epicenter (0.338, 0.186). The calculated CCT from the above equation for L0 and L2 is 4906 K and 4871 K, respectively.

7.3.2.6 TDPL and quantum yield analysis

The investigation of the thermal stability of the phosphor is vital for its technological utilization. In this regard, we have analyzed the thermal quenching phenomenon in the L2 sample. Fig. 7.12 (a) depicts the temperature-dependent PL emission spectra of L2 phosphor in the temperature range of 30℃ – 180℃. It is evident that with rising temperature there is a gradual decrease in the PL intensity. Any shift in the PL spectra is not observed with rising temperatures which is desirable for lighting applications. The decrease in PL intensity with rising temperatures is ascribed to the non-radiative phonon relaxation of the electrons from the higher energy levels [33]. Fig. 7.12 (b) represents the variation of integrated intensity with rising temperatures. The emission intensity at 150℃ is about 56% of the intensity at 30℃. Therefore, there is a 44% loss of emission intensity at 150℃, which is better than some of the reported vanadate phosphors [33,223,240–242]. The influence of the thermal quenching on the emission spectra can be further examined by evaluating the ΔE from the following Arrhenius equation 7.8 [240],

$$I_T = \frac{I_0}{1+Ae^{(-\Delta E/kT)}} \tag{7.8}$$

Where I_0 is the emission intensity at 303K, I_T is the emission intensity at temperature T (Kelvin), k is the Boltzmann constant (8.629 x 10^{-5} eV/K), and A is the constant frequency factor. The $\ln\left(\frac{I_0}{I_T}-1\right)$ vs 1/kT plot, as shown in Fig. 7.12 (c), is linearly fitted and the slope of the fitted line gives the value of ΔE. The obtained value of ΔE is 0.29 eV. The

calculated activation energy of Li^+ doped $Zn_3(VO_4)_2$ phosphor is greater than earlier reported $Zn_3(VO_4)_2$ [199]. The relatively high value of activation energy demonstrates that L2 phosphor has good thermal stability. The good thermal stability of the phosphor is required to avoid overall emission color shifting. The influence of rising temperature on the emission color is explored by examining the CIE chromaticity coordinates of the L2 phosphor at different temperatures. As depicted in Fig. 7.12 (d), there is no remarkable change in the color coordinates under high temperatures. This conclusion is important as stable emission color under working temperatures is desirable for the application of the near UV wLED application. The absolute PL quantum yield of the L2 phosphor was also evaluated with the help of an integrating sphere monitored at 560 nm excitation wavelength and it was obtained as 4.60%.

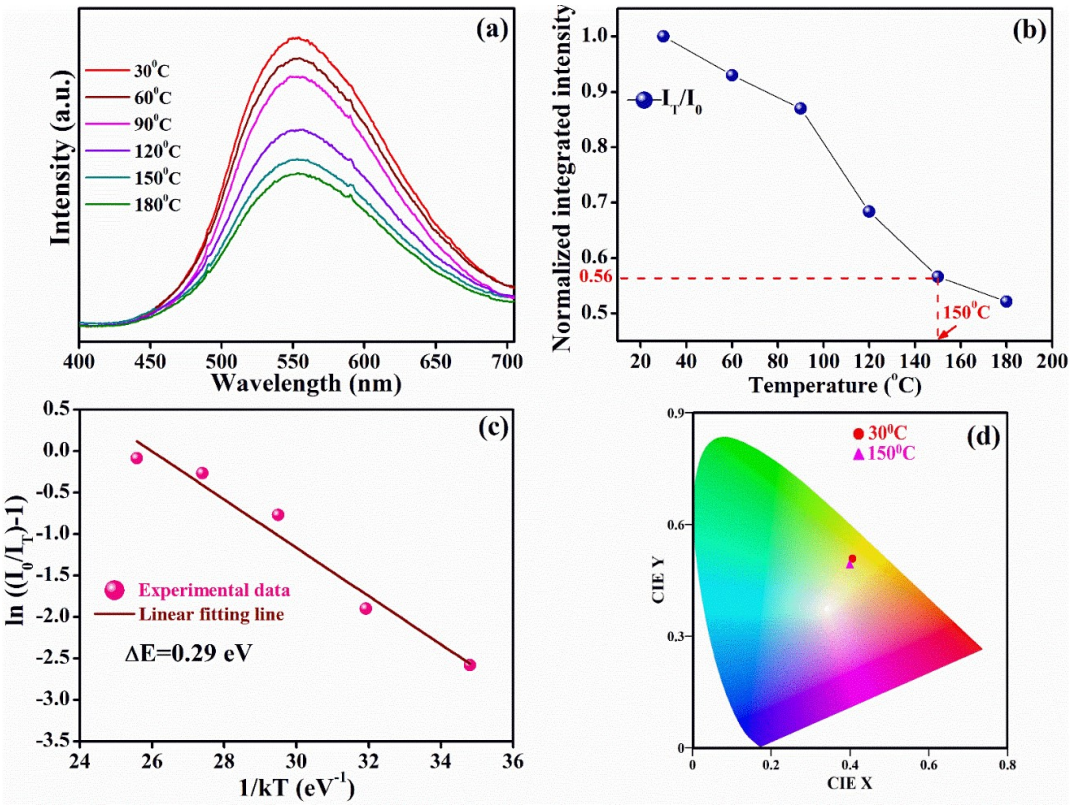

Fig. 7.12 **(a)** TDPL spectra of L2 phosphor, (b) Normalized integrated intensity plot as a function of temperature, **(c)** ln $((I_0/I_T)-1)$ vs. 1/kT plot, and **(d)** CIE chromaticity diagram depicting variation in CIE coordinates with temperature for L2 phosphor.

7.3.2.7 Configurational coordinate diagram

The process of absorption, fluorescence, and thermal quenching in the $Zn_3(VO_4)_2$ can be elucidated by the configurational coordinate diagram depicted in Fig. 7.9 (e). The molecular orbitals of $[VO_4]^{3-}$ in $Zn_3(VO_4)_2$ are expressed as $^1A_1$ ground state and $^3T_1$, $^3T_2$, $^1T_1$, $^1T_2$ excited states [236]. During the process of photoabsorption (360 nm), electrons jump to excited states by following $^1A_1 \rightarrow {}^1T_1$, $^1T_2$ allowed transitions in T_d symmetry. The electrons are relaxed to the equilibrium position in the ^3T state by the process of vibrational relaxation and internal conversion (path (1) in Fig. 7.9 (e)). Due to the spin selection criterion, the $^3T_1$, $^3T_2 \rightarrow {}^1A_1$ transitions are ideally forbidden in T_d symmetry. However, the T_d symmetry is distorted from the idealized tetrahedron and by spin-orbit interaction, the $^3T_1$, $^3T_2 \rightarrow {}^1A_1$ transitions become partially allowed. As a result, the electrons revert to the $^1A_1$ ground state by following path (2) in Fig. 7.9 (e) and giving Em1 and Em2 emission bands (see Fig. 7.9 (b) and (d)). As the temperature is raised, the lattice vibrations are strengthened which increases the thermally active phonons. After coupling with the thermally active phonons, the energy of the excited electrons at the bottom of the $^3T_{1,2}$ band can approach crossover point C. These electrons revert to the ground state non-radiatively by following the path (3) [32]. With the rising temperature, the electron-phonon interaction increases and more electrons cross $\Delta \boldsymbol{E}$ barrier, thereby reaching point C and relaxing non-radiatively to the $^1A_1$ ground state.

7.4 Conclusion

In summary, we have studied the luminescence and structural properties of the undoped and Li^+ doped $Zn_3(VO_4)_2$ successfully prepared by the citrate sol-gel technique. The XRD study ascertains the orthorhombic crystal structure of prepared phosphors, which is well supported by FTIR spectroscopy analysis. The XRD analysis substantiates improvement in

crystallinity for Li^+ doped samples. The W-H plot analysis ascertains an increase in crystallite size for Li^+ doped phosphors. The FE-SEM analysis confirms the augmentation in particle size after Li^+ doping. The XPS examination validates the oxidation states of the elements present in the Li^+ doped phosphor. The excitation of the prepared phosphors lies in the near-UV region and the overall emission is greenish-yellow. Thus, these phosphors can be used with the commercially available near-UV emitting LED chips for the wLEDs application. The Li^+ doping further enhances the PLE and PL intensity of the $Zn_3(VO_4)_2$ phosphors. The increase in emission is accredited to the improved crystallinity, increased particle size, and increased light absorption by Li^+ doping. The decay curve analysis validates improvement in crystallinity which consecutively supports the enhancement in the PL intensity of $Zn_3(VO_4)_2$ as a result of Li^+ doping. The calculated activation energy of the Li^+ doped $Zn_3(VO_4)_2$ is 0.29 eV, validating the good thermal stability of the phosphor. Moreover, there is a 44% loss of emission intensity at 150℃. We conclude that with near UV excitation, greenish-yellow emission, large ΔS value, good thermal stability, and cost-efficient synthesis process, the L2 phosphor is anticipated to be an excellent material for near UV-based white LEDs and other optoelectronic devices.